

CULHAM CENTRE FOR FUSION ENERGY

A Database Study of Unstable Alfvénic and other MHD modes in the JET tokamak

FINAL REPORT

Written by: *Iyngkarran Kumar*

Under the supervision of:
R.A. Tinguely, P.G. Puglia, N. Fil, and S. Dowson

1 Introduction

The successful operation of commercially viable tokamaks in the coming decades will pivot on the ability to achieve and sustain burning plasmas.¹ In the first generation of these devices, the feasibility of operating with a plasma in such a state will depend critically on effective confinement of the 3.5 MeV alpha particle created from the fusion of a deuteron and triton. However, both theoretical prediction and experimental observation have confirmed that unstable Magnetohydrodynamic (MHD) modes possess the ability to rapidly redistribute fast ion populations, including alpha particles, that reside in fusing plasmas, motivating detailed study into their formation, and the mitigation of their effects.

The Alfvén Eigenmode is one such instability; due to its complex interactions with fusion alphas as well as other energetic particle populations such as those accelerated by Ion Cyclotron resonance heating (ICRH) and Neutral Beam injection (NBI), it has demanded the attention of intensive research efforts for a number of decades. The following report outlines a study into these unstable modes, by the means of a statistical analysis of two databases which were compiled from magnetic signals taken from over 2000 plasma discharges conducted in the Joint European Torus (JET), during the 2019-2020 C38 Deuterium campaign. The aim of our study was to discover experimental trends in the data, and compare to predictions made from theory, previous experiments as well as simulation.

We shall begin in section 1 by delving into the theoretical background of Alfvén Eigenmodes, discussing the mechanisms behind their formation in plasmas. In particular, we shall focus our exploration on Alfvénic gap modes with the other types of MHD activity observed during our analysis also briefly mentioned. In section 2, a detailed overview of the compilation of both databases, hereon referred to as Database I and II respectively, will be given. We will see that Database I provides a ‘full pulse’ summary of the 2054 discharges analysed, whereas Database II focused specifically on regions of unstable MHD activity. The mode extraction algorithm (MEA) used to identify such regions will be discussed in depth, followed by the results of a statistical analysis of over 7000 potential instabilities in section 3. We see that our database study is agreeable with analytic theory for the dependencies of mode stability on normalized plasma beta β_N , with stabilizing and destabilizing effects observed for the expected normal modes [4]. Our results associated with mode stability and toroidal mode number (n) are also consistent with past work done in this field[2, 4]. Furthermore, we can discern an unstable mode distribution across frequency space that is in accordance with experimental results given in previous studies [3, 15]. We finish in section 4 with conclusion of our findings, before a consideration of possible opportunities for future work is given.

Before we can proceed, some acknowledgements are in order. I would like to express my gratitude to the supervisor of this internship, R.A. Tingueley, as well as the rest of the TAE team at the Culham Centre for Fusion Energy(CCFE): P. Puglia, N. Fil and S. Dowson. Over the past 11 weeks the knowledge and experience that they have shared with me has been invaluable, and without them this work would not have been possible. For their continuous patience and willingness to assist as I explored their many fields of expertise, I am extremely grateful. Finally, I thank the CCFE as well as the UKAEA² for the coordination of this internship.

This work has been carried out within the framework of the EUROfusion Consortium and has received funding from the Euratom Research and Training Program 2014–2018 and 2019–2020 under Grant Agreement No. 633053. The views and opinions expressed herein do not necessarily reflect those of the European Commission.

This work was funded by the RCUK Energy Programme [Grant number EP/T012250/1]

¹These are confined plasmas with a significant proportion of the heating power coming from fusion born products, as supposed to external sources.

²United Kingdom Atomic Energy Authority

2 Alfvén and other MHD eigenmodes

We will begin with a brief study of the various normal modes seen in a tokamak, with a particular concentration on the Alfvén Eigenmode (AE). Often used in tokamak science is the coordinate system shown in Figure 1 which uses the variables R (major radius), r (minor radius), ϕ (toroidal angle, in JET this is measured from octant 1, see [5]), θ (poloidal angle) and z (vertical height from midplane); from now on we will also employ this system.

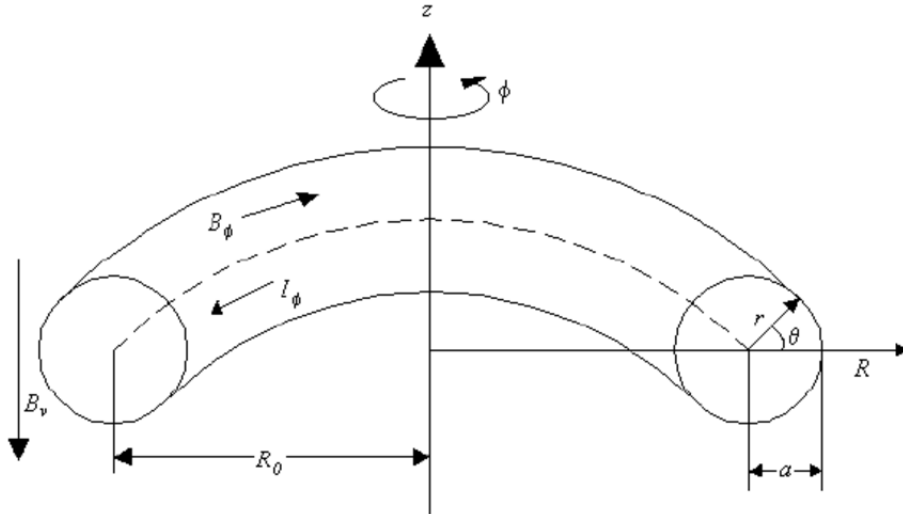


Figure 1: Geometry of a conventional tokamak

Alfvén waves, first theorised in 1942 by Hannes Alfvén [1], are electromagnetic waves observed at low frequencies in an electrically conducting fluid that is in the presence of an equilibrium magnetic field. Three types exist, but we shall be primarily concerned with the shear Alfvén wave, or SAW; this is an incompressible wave travelling parallel to magnetic field lines, where the restoring force is provided by magnetic field tension. The dispersion relation of the SAW is given below as equation 1a; here V_A is the aptly named Alfvén speed at which the SAW propagates through the plasma. As usual, ω is the angular frequency of the wave, k_{\parallel} the wave number ($= \frac{2\pi}{\lambda_{\parallel}}$), μ_0 the vacuum permeability and $\sum m_i n_i(r)$ the effective ion mass density of the fluid, referred to as m_{eff} from hereon. $B_0(r)$ in equation 1b denotes the on-axis magnetic field, and q in 1c the tokamak safety factor, discussed further in section 4.

$$\omega = k_{\parallel} V_A \quad (1a)$$

$$V_A = \frac{B_0(r)}{\sqrt{\mu_0 \sum m_i n_i(r)}} \quad (1b)$$

$$k_{\parallel} = \frac{nq - m}{R_0 q} \quad (1c)$$

We note the explicit dependence of the Alfvén speed (and subsequently the dispersion relation) on tokamak minor radius. This yields a spatial profile like that in Figure 2a (This figure has toroidal mode number, n, and poloidal mode number, m, both equal to 4) for the normalised frequency of the SAW, known as the Alfvén continuum. The shape of this profile provides the reason as to why SAWs are difficult to excite. Radially adjacent regions will have different phase velocities, resulting in shearing that rapidly disperses the wave, known conventionally as continuum damping, which is proportional to the magnitude of the gradient of the Alfvén continuum [15]. Subsequently in most instances, SAWs fail to grow to any noticeable amplitude.

However, under certain conditions such an event can occur, giving rise to Alfvén Eigenmodes (AEs). Whilst the ways in which this can happen are numerous, we shall explore the formation of the toroidicity-induced AE (TAEs) in detail and only briefly discuss other types of AE at the end of this section. The interested reader may refer to section 2 of both [10] and [15] for a more comprehensive discussion of reversed-shear AEs (RSAEs), TAEs, ellipticity-induced AEs (EAEs), noncircularity-induced AEs (NAEs), beta-induced AEs (BAEs) and the rest of the Alfvén ‘zoo’.

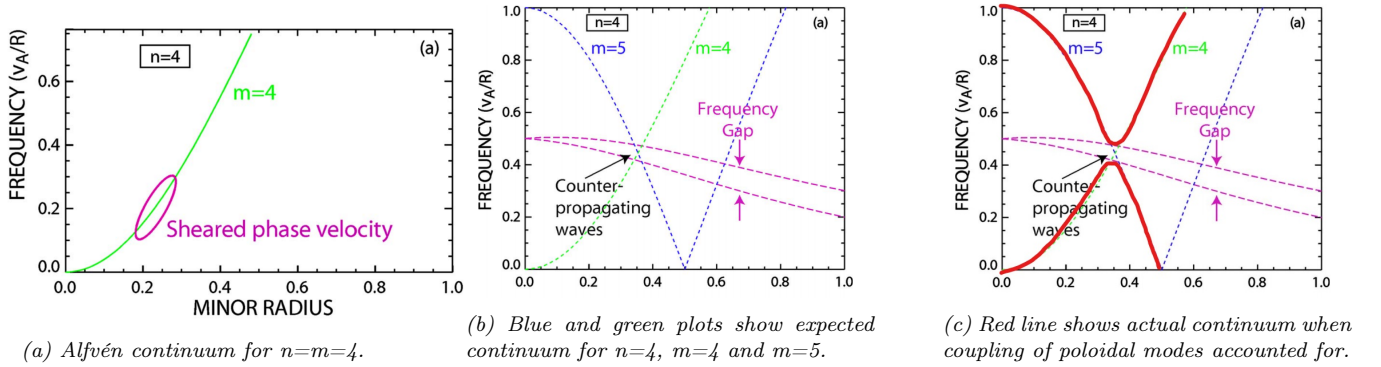


Figure 2: Various Alfvén Continua. Taken/adapted from Figures 1 and 2 in [15]

The appearance of the TAE can be accounted for by considering the interaction of poloidal components of two SAWs with the same toroidal mode number (n), but poloidal mode numbers differing by one (m and $m+1$ say). One may expect the Alfvén continuum of the modes to be that shown in Figure 2b, but this is not the case; instead that of Figure 2c is obtained. This result may seem initially surprising but can be explained by the fact that the refractive index of a plasma is periodic along the toroidal axis (with period 2π radians) as well as noticing that two SAWs as described above will be counterpropagating (see equation 1c). Upon appreciation of this, we see that the phenomenon of Bragg reflection will lead to a ‘frequency gap’ in the dispersion relation, centered at $f = f_{TAE} = V_A/4\pi qR_0$. This frequency gap can be seen in Figure 2c. The TAE then forms at and around the local extrema of this Alfvén continuum, due to the significant lack of continuum damping that we recall is proportional to $\frac{\partial V_A}{\partial r}$.

In the following analyses we shall come across several AEs and other MHD modes that appear as a result of different physical processes. These are listed below, for completeness:

- The ellipticity-induced AE (EAE) and the noncircularity-induced AE (NAE) are the results of analogous processes of that which leads to the TAE, except poloidal harmonic coupling occurs between m and $m+2$ for EAEs and m and $m+3$ for NAEs. The ellipticity and noncircularity of a tokamak plasma cross-section and the subsequent coupling of poloidal modes m and $m+2$ and/or m and $m+3$ lead to further frequency gaps at $f = 2f_{TAE}$ and/or $3f_{TAE}$ respectively. The AEs that result from the formation of frequency gaps are often referred to as ‘gap modes’.
- The RSAE is seen at the extrema of the q profile [15], which coincides with the extrema of the Alfvén continuum. Once again, the absence of continuum damping here allows for the presence of the RSAE. Related also to the minima of Alfvén continua are the global AEs (GAEs). These exist at frequencies just *below* the minimum, and can be excited by energetic particles [10]. Continuum damping is avoided as $\frac{\partial V_A}{\partial r} = 0$ for GAEs. Both the RSAE and GAE frequencies are similar to that of TAEs and EAEs.
- The beta-induced AE (BAE) is a normal mode that owes its existence to the frequency gap often seen in a plasma with finite plasma beta (plasma beta, β , is the ratio of plasma kinetic pressure to magnetic pressure. It is classified finite if $B > 0$) [4]. This frequency gap is seen at $f \approx f_{TAE}/2$.
- (Neo-) Classical tearing modes are not AEs, but another type of MHD instability driven by free energy inherent in current and pressure profiles, in a resistive plasma only.

3 Methodology

We shall now provide an overview of the methods used to compile both Database I and Database II. To begin with, a brief discussion is given on the probes system used to capture the magnetic field perturbation data from a JET plasma.

3.1 Fast Magnetic Probes (FMP) system

The formation of MHD eigenmodes in the JET plasma leads to perturbations in the surrounding magnetic field which are recorded by a number of probes situated around the tokamak. These fast magnetic probes operate at a sampling frequency of either 1.0 MHz or 2.0 MHz, resulting in a Nyquist Frequency³ of 500kHz or 1000kHz. For this work, we took data from 21 of these diagnostics; 6,7 and 8 probes from the *T0XX*,*H3XX* and *PP8XX* families respectively, with the locations of some of these given in the table below:

Probe	T001	T008	H303	H305	PP801	PP803	PP805	PP807
<i>R</i> (m)	3.868	3.862	3.876	3.877	3.766	3.954	3.863	3.447
<i>z</i> (m)	1.002	1.016	1.000	1.006	1.248	0.692	-0.385	-1.059
ϕ (°)	3.000	257.1	77.00	107.3	154.8	154.6	154.7	155.2

Please see [5] for visuals of the probe geometry. Here we should mention that the *T0XX* and *H3XX* families are located at a number of toroidal locations around JET, but at a fixed poloidal location whereas the converse holds true for the *PP8XX* family. This makes the *T0XX* and *H3XX* probes adept for the calculation of toroidal mode number only, with the *PP8XX* probes instead used to calculate poloidal mode number, as will be seen in section 3.2.1.

Each probe returned a time signal of the rate at which the magnetic field was being perturbed with respect to time. From the recent 2019-2020 JET C38-D campaign, we processed data from the pulses in which (*i*) Ion Cyclotron resonance heating (ICRH) power[11] exceeded 500kW for 100 milliseconds, considering the time interval bounded by the first and last instances in which (*i*) was satisfied. This was done to ensure that the analysis was conducted solely on intervals in which MHD activity was to be expected; previous operational experience indicates that this is not the case for ICRH powers less than 500 kW.

A Fourier decomposition was then performed on the filtered signals using a time bin length of 2.048ms (T_{bin}), yielding a spectrogram matrix⁴ of complex Fourier amplitudes spanning a frequency range $f_{min} < f < f_{Nyquist}$. The minimum resolvable frequency f_{min} was calculated as the inverse of the time bin length, below which there are insufficient wave cycles in each time bin to accurately compute a discrete Fourier transform. Indeed this is why the time bin length given above was selected, as it provided a satisfactory compromise between a high frequency resolution ($\propto T_{bin}$) and a low f_{min} ($\propto \frac{1}{T_{bin}}$). In this work, $f_{min} = 0.488\text{kHz}$.

3.2 Database I

We now take the opportunity to document the process by which Database I was compiled. A discussion of the methods used to create a list of four spectrograms associated with each pulse is undertaken first.

3.2.1 Spectrograms

For each pulse the Fourier amplitude spectrograms from all probes⁵ were used to construct the four spectrograms listed below. The results are also given for a sample pulse JPN 94700 in Figures 3 and 4.

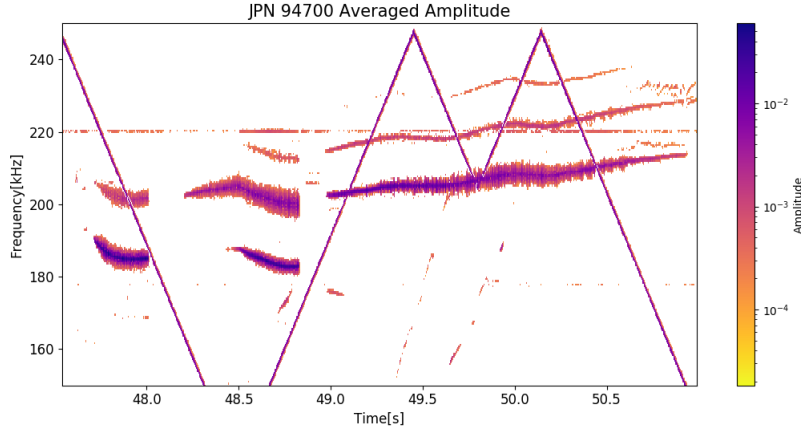
- An ‘Averaged Coherence’ spectrogram matrix - For N probes, we found all possible pairings of probes (a total of $\binom{N}{2}$). A coherence calculation was then performed on each pairing; this returned a spectrogram that only included signals recorded by *both* probes. These $\binom{N}{2}$ coherence matrices were then averaged to give the Averaged Coherence spectrogram, which contains signals seen by *all* probes. Finally, all signals in the coherence matrix with coherence less than 0.6 (threshold chosen heuristically) were set to 0. Please see Appendix A for a more detailed discussion of the motivation behind and method of the coherence calculation. Figure 3b shows a plot of the Averaged Coherence spectrogram obtained for JPN 94700.

³This is the maximum frequency a probe can resolve, $f_{Nyquist}$. For a sampling rate of f_s , $f_{Nyquist} = f_s/2$

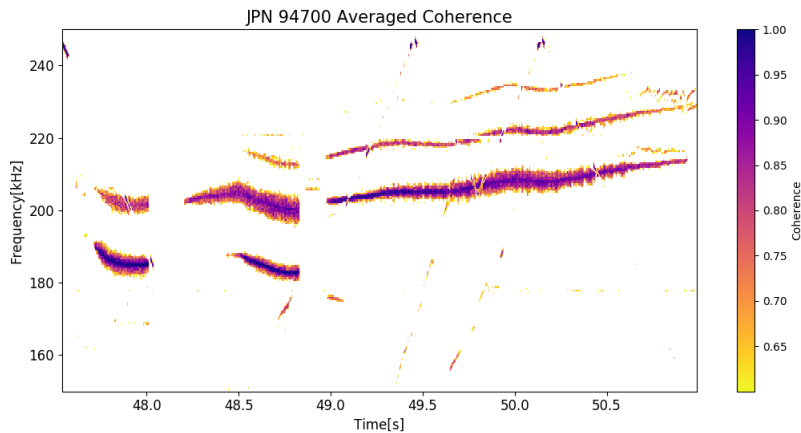
⁴A matrix is the optimal discretised representation of a spectrogram. The ijth element of a spectrogram matrix is the complex amplitude of the ith Fourier mode in the jth time bin

⁵Occasionally some probes did not return a time signal, therefore they did not contribute to the pulse spectrograms. FMP *H308* rarely returned a signal

- An ‘Averaged Amplitude’ spectrogram - This was obtained by averaging the amplitude spectrograms over all probes. See Figure 3a; however note that the final amplitude matrices stored in Database I had the Alfvén Eigenmode Antenna Diagnostic (AEAD) and ICRH signals removed. These can be seen in Figure 3a as the triangular waveform and the signal localised at $f = 220\text{kHz}$ and are included solely for comparison with Figure 3b.



(a) Amplitude spectrogram with ICRH and AEAD signals included.



(b) Averaged Coherence spectrogram. Contains only the signals recorded by all probes.

Figure 3

- A toroidal mode number spectrogram - For each nonzero index in the Averaged Coherence matrix (recall that those signals with coherence less than 0.6 were set to 0), the toroidal mode number (n) was estimated by means of the minimisation of a weighted, reduced Chi-Square calculation, given by equation 2 (see [9]). We note that The range of toroidal mode numbers considered was $-1 \leq n \leq 8$ ⁶, referred to as n_{range} hereon, with the choice of n_{range} justified by past experimental results in which modes with n lying outside the interval are rarely seen. See Figure 4a.

$$\chi^2(n) = \frac{1}{N^2} \sum_{i=1}^N \frac{\sum_{j=1}^N \frac{\min[n(\phi_i - \phi_j) - \theta_j]}{\sigma_j^2}}{\sum_{j=1}^N 1/\sigma_j^2} \quad (2)$$

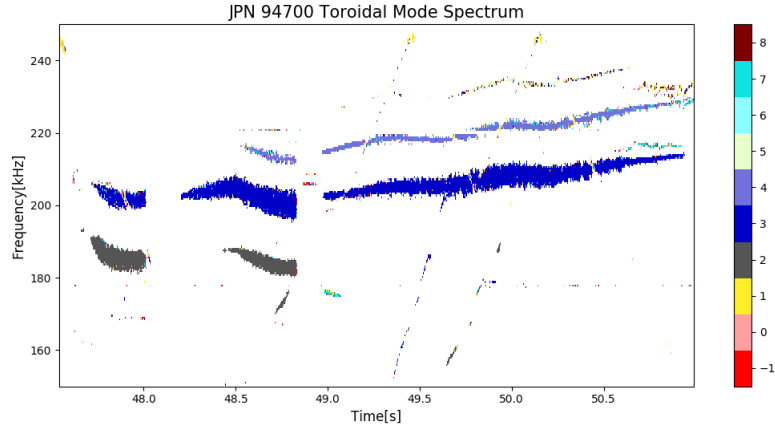
- A poloidal mode number spectrogram - Akin to the toroidal mode number calculation, an index was assigned poloidal mode number m if m minimised $\chi^2(m)$ for $m \in m_{range}$ ⁷. m_{range} was chosen as $-1 \leq m \leq 24$ again due

⁶This however is certainly not the maximum resolvable mode number of the Chi-Squared calculation; see Appendix A of [9] for a comprehensive discussion of this.

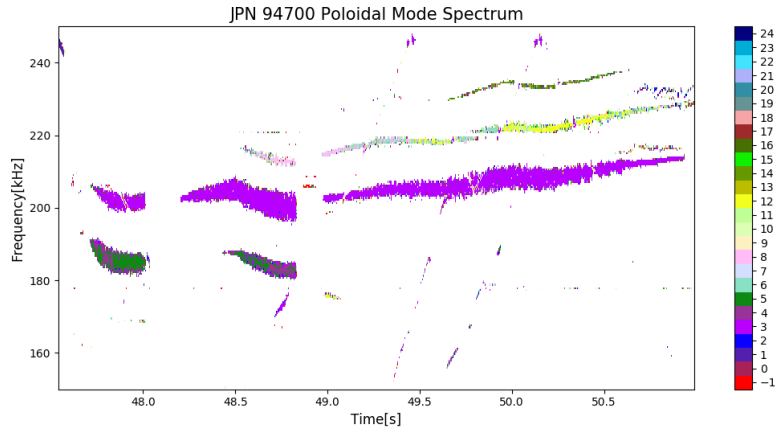
⁷Due to the nature of some AEs, which are associated with multiple m , the Chi-squared calculation may not be the optimal method

to the fact that the probability of seeing modes with poloidal mode number m outside this range is low. The choice of n_{range} and m_{range} allows for the identification of Alfvénic waves up to the $q=3$ flux surface. See Figure 4b.

Given that the plasma centroid⁸ varies as a function of time, and the accuracy of the signal recorded by a FMP decreases with the distance between the probe and signal origin, we introduced an uncertainty σ for each probe equal to its distance to the centroid ($d_{centroid}$) that was factored into the Chi-Square calculation. This is not required for the toroidal mode number calculation, as $d_{centroid}$ remains roughly constant for the $T0XX$ and $H3XX$ families.



(a) Spectrogram of toroidal mode numbers.



(b) Spectrogram of poloidal mode numbers. Note the 50/50 assignment between $m=4$ and $m=5$ for apparent gap modes located at $f \approx 180\text{kHz} - 190\text{kHz}$, and $t \approx 47.5\text{s} - 49.0\text{s}$.

Figure 4

All signals returned by probes include the signature of radio frequency (ICRH) heating, as well as that of the AEAD antenna [12]. These were removed from the spectrograms in post-processing by reconstructing the signals and subtracting from the Averaged Coherence matrix, which can be seen in a comparison between Figure 3a and Figure 3b.

3.2.2 Plasma and Operational Parameters

To probe trends in properties of unstable Alfvén and other MHD modes, 27 parameter time signals (taken over the same time interval that the spectrograms covered and interpolated to give an identical time resolution) were also added to the database entry for each pulse. Please see Table 3 of [9] for a list of these.

to calculate mode indices. However alternate methods, such as Sparse Spectral Decomposition [13], proved to be too computationally intensive for $\sim 10^5$ indices per pulse.

⁸The centre of the plasma as weighted by the spatial plasma current profile.

3.3 Individual Mode Database

To conclude this section, we shall highlight the methods employed to construct a database of individual mode characteristics (Database II) from the spectrogram database previously described. It was this database that was used to carry out the bulk of the analysis in the next section, therefore it was of great importance to ensure that the way in which modes were identified was done to a high level of accuracy. We will see that the main challenge to this was to remove the effects of noisy signals that survived the coherence calculation. The extent to which modes were successfully identified will be evaluated at the end of this section, with Figure 6 to support.

Mode Separation: To initialise the process of identifying individual modes and the accompanying characteristics, for each toroidal mode number n , we applied a simple frequency/time separation algorithm on the nonzero indices with mode number n in the Averaged Coherence spectrogram. The indices were ordered by frequency, and those that were separated by 1.5 kHz or more were classified as being different structures in frequency space. Following this, the indices in each frequency structure were then separated in time, with adjacent indices considered part of the same time structure if they differed by 40 ms seconds or less.

Time filter: The next step was to remove any identified structures in the frequency-time space that existed for 75 ms or less. These transient signatures were almost always noisy signals. Before continuing, we emphasise the fact that the 75 ms threshold, as well as the thresholds discussed in the rest of this section, were **heuristically chosen** and there remains room for their optimisation.

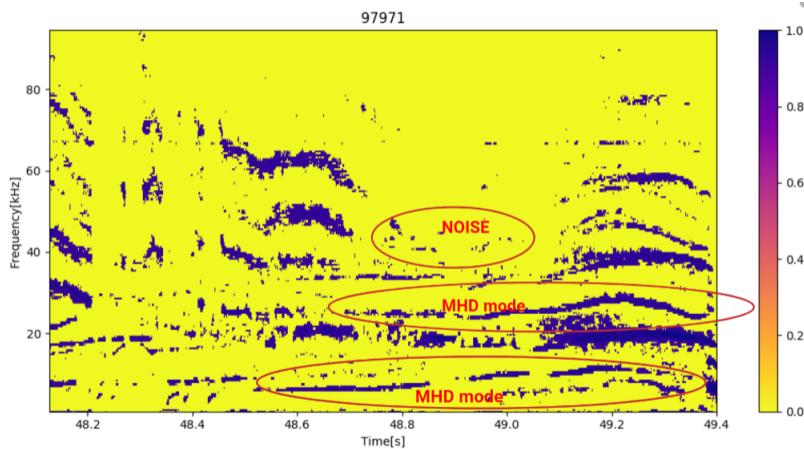


Figure 5: A particularly active region of JPN 97971, highlighting the need for filtering. Only two of the MHD modes present are highlighted, but evidently these are not the only instabilities present.

Percentile Truncation: Remaining structures underwent a truncation of their extreme index values; indices lying outside of the 5-95 percentile range for frequency or time were removed. For the majority of structures this removed noisy indices that had been incorrectly captured at the ends; however for well separated modes this procedure would have cut off ‘valid’ indices. We note that this could be a source of small inaccuracy for our algorithm.

Index density filter: The observation that noisy signals were much sparser in the frequency-time space than MHD modes motivated an index density filter to be implemented that was effective in removing noisy signals. Structures that had less than 0.1 indices per unit area were eliminated⁹.

Area filter: Structures that covered a space on the frequency-time plane that was less than 500.0 units squared (512.0 Hertz-seconds) were removed from the mode identification process. Those with areas below this threshold were most often noise signatures.

ICRH filter: One may notice from Figure 6a that for some pulses, not all ICRH signals were removed during postprocessing. Whilst it was possible to remove both beating and aliasing signatures, those that resulted from a combination of beating and aliasing signals would have taken considerable further work to eliminate. To ensure that these were

⁹The calculation of index density assumed a uniform distribution of indices across the area covered by the structure. Structure area was found in an identical way to the method used in the area filter discussion

not identified as MHD modes, we made use of the high degree localisation of ICRH signals in frequency space and eliminated all signals that span a frequency range of 3.0 kHz or less.

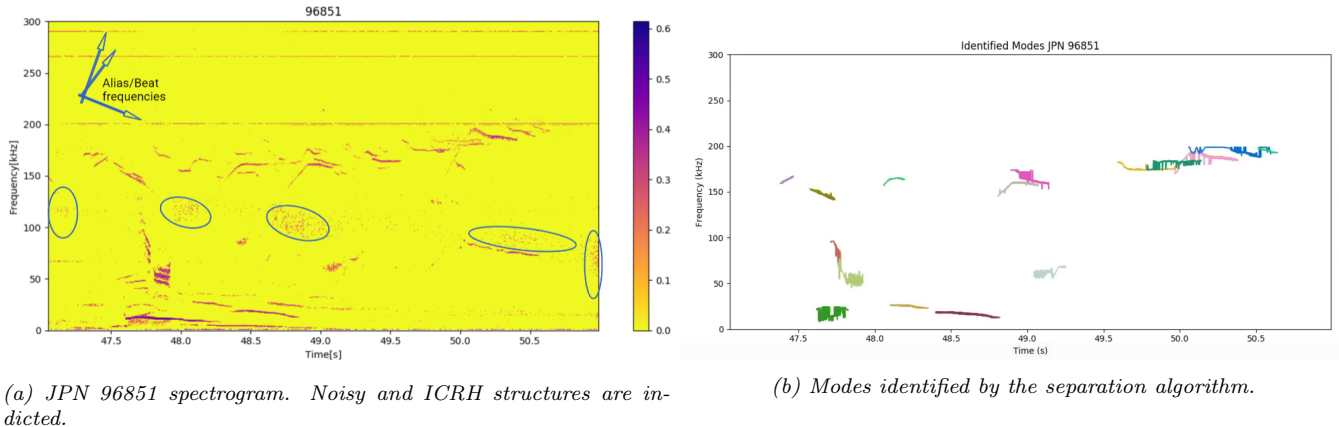


Figure 6

The plots above show the results of the extraction algorithm on sample pulse JPN 96851. We see that the mode extraction algorithm (MEA) is able to deduce the main structures present in the spectrogram, but there is space for optimisation of the various thresholds. We also note that the MEA is more adept at identifying certain types of MHD modes over others. For example, it has a high chance of finding TAEs and NTMs as these modes are *relatively* localised in frequency space compared to the RSAE for example, which due to its frequency chirping¹⁰, is sometimes assigned a low index density and removed from the identification process. Modes ‘cut up’ by regularly occurring sawtooth crashes¹¹ may also be prone to inaccurate identification.

A final comment should be made regarding the frequency space from which the MEA extracted modes. Although most spectrograms were constructed for frequencies in the range 0-1000kHz, we applied the MEA to the 0-500kHz space only. We observed that the 500-1000kHz band was mainly composed from ICRH and noise signals, and there was little MHD activity. From this it was decided that the reduction in confidence of our results from extracting potential MHD activity from this range exceeds the gain from the physical insight we would obtain, hence the reason for the truncation of the frequency space.

3.3.1 Mode characteristics and parameters

We conclude the discussion of the MEA by reviewing the characteristics that were assigned to each identified mode (IM) in the database. These are listed below:

- Each IM was assigned the toroidal mode number n that was calculated from the indices that comprised it.
- The poloidal mode number distribution of the IM was deduced. As gap modes often are comprised of multiple poloidal harmonics, a list of values of m were associated with each IM, with mode number m being included if 25 percent (or more) of the spectrogram indices that define the IM had mode number m ¹². The proportion of the indices in the IM that had mode number m was also stored, allowing one to calculate a weighted value of m .
- A 5 element array of times was associated with each IM ($t_5, t_{med}, t_{95}, t_A, t_{pulse}$). t_5 is the 5th percentile value of the time interval the IM was present, (an indication of the time that mode was roughly first seen), t_{med} is the median time of this interval, t_{95} the 95th percentile value of the same time interval (an indication of the time that the mode was last observed), t_A the time at which the maximum amplitude of the mode is first seen and t_{pulse} the start time of the *pulse* signal (the time at which the pulse first exceeds ICRH power of 500kW).
- A 4 element array of frequencies is also given, ($f_5, f_{med}, f_{95}, f_A$). They are defined analogously to the time array above, but of course in frequency space.

¹⁰Occurs for the RSAE as the minimum of the q profile varies with time, characterised by rapidly changing mode frequency. See equation 3 of [2]

¹¹Quasi-periodic flattening in the radial temperature and density profiles, triggered by magnetic reconnection events in the plasma core. See [8] for the effects on Alfvén Eigenmodes

¹²Those with less than 25 percent were discarded. We believed that a mode identified to be composed of ~ 4 harmonics was likely due to an inaccurate Chi-Squared calculation. However, such modes can exist in plasmas (see footnote 18), but are rare.

- A_{max} , the maximum amplitude of the IM is found from the ‘Averaged Amplitude’ matrix.
- We also associate time averaged plasma and operational parameters with each IM. The parameters given in rows 1-6,9-11 and 15 of Table 3 in [9], as well as n_{95} , edge electron density, ∇n_{95} , edge electron density gradient, and the KA3 signal, a proxy for fast ion losses, were averaged over the time interval of the mode *and* 100ms, 250ms and 500ms prior. The 3 intervals above are roughly the times for a range of fast ions seen in JET to equilibrate. [16].

4 Statistical Analysis

Database I contained 2054 JET pulses from the 2019-2020 JET Deuterium campaign, C38-D, spanning JPN 93190 - 98005. Database II, constructed from the application of the mode extraction algorithm (MEA) (Section 3.3), consisted of 7179 MHD modes identified in these pulses. The following section highlights our findings from analyses of these, in which generally good agreement with theoretical prediction is observed, as well as some unexpected results that will require further exploration.

4.1 Exploration of Mode Distributions

To initiate our study of the identified modes in Database II, an insight into the location of MHD activity across frequency space was pursued. Results are shown in Figure 7:

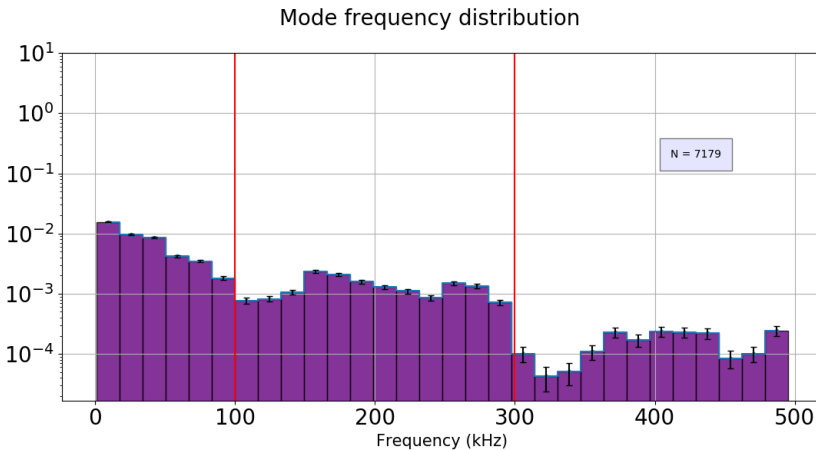


Figure 7: Frequency distribution for modes in 0-500kHz range.

Three distinct bands can be seen, indicated by the red vertical lines; these are the 0-100kHz, 100-300kHz and 300-500kHz bands (referred to as low, intermediate and high bands in subsequent discussions), which correlate well with theoretically predicted Alfvénic and other MHD waves. We expect that the low band is populated by NTMs, BAEs, BTGs (beta-induced ion temperature gradient driven eigenmodes); TAEs, GAEs and RSAEs and low frequency EAEs to reside in the intermediate band, and TAEs, EAEs as well as low frequency NAEs to be found in the high band.

It is worth noting that the number of modes in the low band exceeds the number in the intermediate band by over 3000, with an order of magnitude difference between the intermediate and high bands (see below for exact numbers). However given the nature of the various driving mechanisms for the aforementioned MHD modes, this result is to be expected. The Alfvén Eigenmodes that are predicted to exist in the intermediate and high bands require a significant fast ion population¹³ (seen only in the presence of high Neutral Beam Injection (NBI) and Ion-Cyclotron Resonance Heating (ICRH)), to be driven unstable by means of wave-particle resonances [14], whereas the NTMs and BTGs seen in the low band merely require pressure and current gradients that are readily found in the thermal population of the plasma.

The discrepancy between the number of modes in the intermediate and high bands may be due to the fact that the wave-particle resonance condition, equation 3 of [14], is more often satisfied for TAE frequencies than for higher frequency gap modes.

We shall now study parameter/mode characteristic trends seen across Database I and II. The lack of observed MHD activity in the high band (~ 180 identified modes, compared to ~ 1900 and ~ 5000 for intermediate and low bands respectively) means that it is not included in further discussions until more pulses are added to the Database(s).¹⁴

4.2 Normalized Beta, β_N

Figure 8a depicts the normalized database histograms across the normalized plasma beta, β_N , given in (3) with β as the conventional beta parameter (the ratio of mean plasma pressure, $\langle p \rangle$, to the magnetic pressure associated with

¹³These are energetic particles with energies ranging from $\sim 10^2$ keV (e.g. NBI ions) to a few MeV (fusion-born alpha particles and ICRH accelerated ions)

¹⁴We hope to analyze data from recent H,D and DT campaigns.

the mean magnetic field in a tokamak, $\langle B \rangle$), a as the device minor radius, B_T the toroidal magnetic field and I_p the plasma current.

$$\beta_N = \beta \frac{aB_T}{I_p} \quad (3)$$

The top image is that for Database I (the 2054 β_N time arrays were inputted to create the histogram), and the bottom two are the low and intermediate bands as discussed above, taken from Database II. One can view the Database I plot as an indication of the parameter distribution across *all* times, whereas the Database II plots focus on the times at which modes are found by the MEA. Of interest here is the evolution of the intermediate band plot as we progress to higher β_N ; the number of identified modes decreases as β_N increases suggesting that MHD activity in the 100-300 kHz range is more localised at low β_N . We note that this is in accordance with equations 12 and 14 in [3], where the expressions for TAE damping from ICRH fast ions, NBI particles and bulk ions (ion Landau damping) exhibit a linear dependence on β_f , β_b and β_i respectively. Here the toroidal plasma beta of species s , β_s , is the ratio between plasma pressure due to this particle species and toroidal magnetic field pressure. f denotes the ICRH fast ions species, b the NBI beam particles and i the thermal ion species.

Another dependence on normalized plasma beta should be highlighted. Figure 8b indicates a generally increasing trend between the maximum amplitude attained by the identified modes in the 0-100kHz frequency band, and β_n . Recalling that the BAE and other beta-induced waves are likely to reside in this band, we refer to [4], with Figure 15 in this paper especially relevant. Experimental results from the DIII-D tokamak are given here, with a dependence of BAE stability on poloidal beta, $\beta_p \propto \beta_N$ seen. Physically, two justifications are given for decreased BAE stability (and subsequently higher mode amplitude). A high β opens up a larger frequency gap in the Alfvén continuum, leading to reduced continuum damping. In addition to this, larger β suppresses the formation of higher frequency TAEs and RSAEs [4]. These higher frequency modes are known to lead to the flattening of fast-ion distribution gradients ($\partial f / \partial r$, $\partial f / \partial E$), therefore the absence of these ensures that free energy from such gradients is readily available to drive the BAE unstable.

We should note that the presence of neo-classical tearing mode (NTMs) driven by pressure gradients in the thermal population of the plasma further supports the result in 8b, given that β_N is proportional to plasma kinetic pressure.

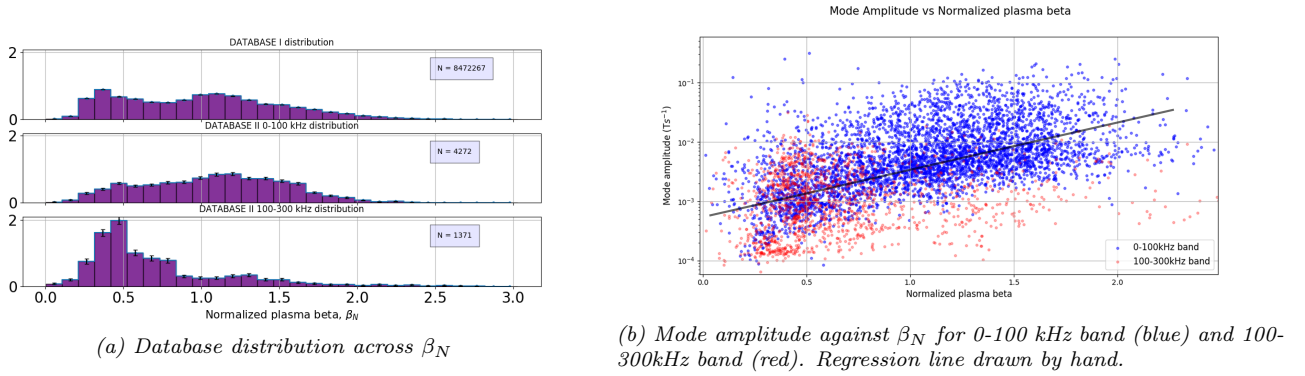


Figure 8

4.3 Toroidal mode number, n, and safety factor, q

Our discussion is now redirected to a consideration of the distribution of modes across the space of possible toroidal mode numbers, as well as the safety factor (q) distribution.

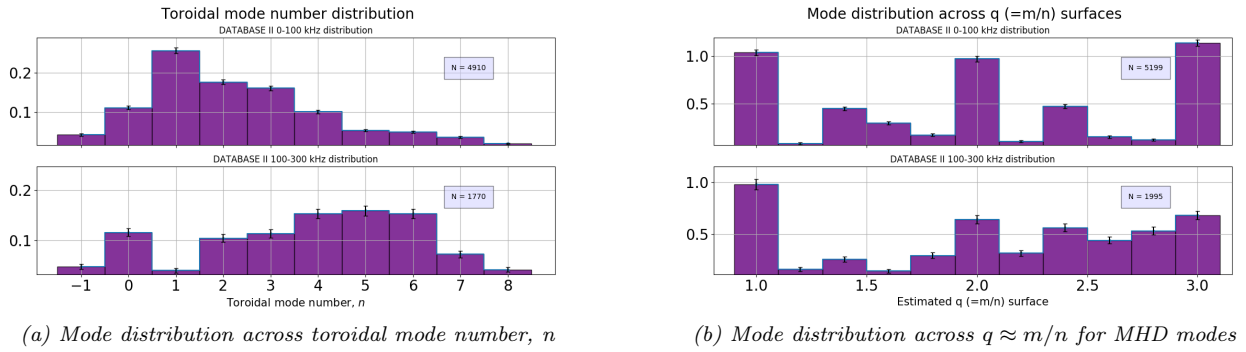


Figure 9a (once again, a normalized histogram) reveals that there is indeed a dependence on the stability of MHD modes on toroidal mode number, in both the low and intermediate band. For the 0-100kHz band, $n=1$ modes are most commonly seen with the frequency of observation falling monotonically on either side of this value. Recalling that magnetic field line tension f_B acts as a restoring force for the the SAW (shear Alfvén wave) and therefore the Alfvén Eigenmode, (where $f_B = \frac{1}{\mu_0}(\vec{B} \cdot \nabla)\vec{B}$ [7]), we see that modes with lower n (and hence lesser $|\nabla\vec{B}| \propto f_B$) will be more easily perturbed and driven unstable.

The trend is quite different for the intermediate band, in which $n=5$ modes are seen most often. The question of optimal n for mode instability is not as simple as for the low frequency band. As previously mentioned, the stability of Alfvén gap modes is highly dependent on the driving and damping mechanisms that result from fast ion species present in the plasma¹⁵, with the ratio of the driving to damping rate for a fast ion species s , $(\gamma/\omega)_s^{net}$ say, proving to be the critical parameter when judging the net effect of the species. It is seen that $(\gamma/\omega)_{ICRH}^{net}$ and $(\gamma/\omega)_{NBI}^{net}$ both display proportionality with n [3], which directly opposes the tendency for low n modes to be the most unstable. Further to this, it should be known that there is also a relation with mode stability to mode width (commonly denoted as Δ_m , with $\Delta_m \propto 1/n$) and fast ion Larmor radius r_L ¹⁶. It is seen that alpha particle drive increases for r_L in the range $0 \leq r_L \leq \Delta_m$, peaks at $L_r \approx \Delta_m$ and declines past this point (see Figure 5 of [6]).

A study of the interplay between these three factors, and potentially others that are not discussed here, leads to equation (4); the predicted n for which AEs are most stable, or $n_{unstable}$.

$$n_{unstable} = \frac{aB_T Z_f e}{q\sqrt{8E_f m_f}} \quad (4)$$

Here a is tokamak minor radius (Figure 1), B_T the toroidal magnetic field, Z_f , E_f and m_f the atomic number, energy and mass of the fast ion, e the elementary charge, and q the safety factor estimated at $r = a/2$. For fast ion energies of 1 MeV, and $q=2$, for JET we do indeed find $n_{unstable} \approx 5$.

A peak in the toroidal mode number distribution is also seen at $n = 0$, for which there are two plausible justifications. It is shown in equation 2 of [2] that for fast ion velocities V_A , $n = 0$ modes are driven strongly due to energy gradients in the ion distribution function. However, the peak could be a consequence of the Chi-Squared calculation (equation (2)) used to estimate mode numbers, which will often assign $n = 0$ if n is not well defined for an observed instability.

The estimated location of the frequency bands across q surfaces (see below) is given in Figure 9b. First of all, we take this chance to remind/inform the reader that the safety factor, q , is a metric for the rotational transform of a magnetic field line, described as the number of toroidal revolutions required by the field line in order to complete one poloidal rotation. In tokamak science, ‘ q surfaces’ are defined as magnetic flux surfaces over which the safety factor is constant. q is estimated for normal modes as m/n , with m and n once again poloidal and toroidal mode numbers; hence we observe the unstable modes at rational q surfaces¹⁷. Upon recalling that a significant number of unstable MHD waves are seen with $n = 1$ (Figure 9a), the predominance of integer q surfaces (e.g. $m/n = 1/1, 2/1, 3/1$) in Figure 9b is accounted for. The more even spread for the 100-300 kHz band may be accounted for by the nature of the gap modes seen at these frequencies, where there can be *two* m associated per mode¹⁸. However, large gradients in the fast ion distribution between the $q = 2$ and $q = 3$ surfaces could provide the free energy needed to return a similar result, so further work may be needed for this to be determined.

¹⁵Neutral beam ions, ICRH ions and fusion-born alpha particles are examples

¹⁶This is the gyroradius for a fast ion orbiting about a magnetic field line

¹⁷Modes located at $q = m/n$ reconnect on themselves after n rotations

¹⁸Some gap modes can have several poloidal harmonics associated. The global toroidal Alfvén Eigenmode is an example, where frequency gaps are opened in the Alfvén continuum for *multiple* pairings of poloidal harmonics ($m - m+1, m+1$ and $m+2, m+2 - m+3$ etc)

4.4 Additional trends

To close this section we shall mention some further trends observed during our analysis that were not covered in the discussions above. Each result is given with the figure that highlighted the trend and a few brief comments.

4.4.1 External Heating Power

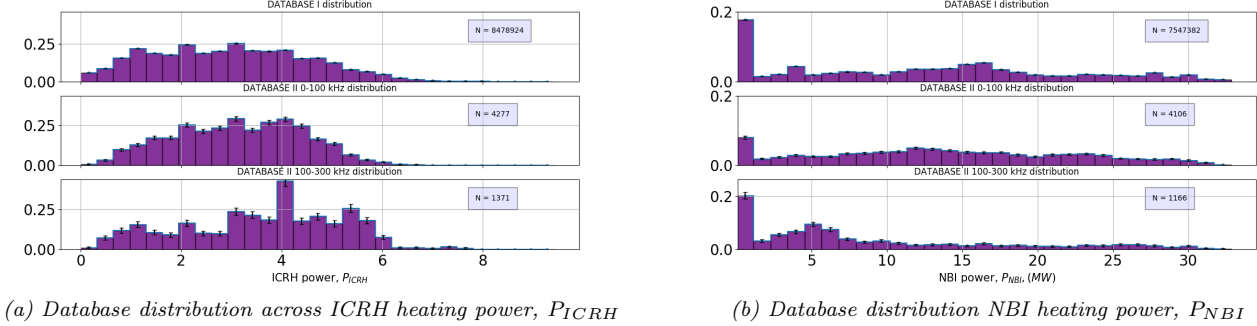


Figure 10

The Figure above gives the normalized histograms for distribution across ICRH heating power, P_{ICRH} , as well as NBI heating power, P_{NBI} . In the JET tokamak, it is seen that $\gamma_{ICRH}^{drive}/\gamma_{ICRH}^{damp} \gg 1$ [3], justifying the shape of the intermediate frequency band in Figure 10a. Modes are most commonly identified at $P_{ICRH} > 4\text{MW}$, in stark contrast to the power distribution across *all* times (top plot in the figure). Table 1 in [3] can be referred to for a quantitative overview of the effects of NBI heating power on Alfvénic waves in JET, for which we see the net effect on gap modes is damping; as indicated by Figure 10b.

4.4.2 Central electron temperature, T_{e0}

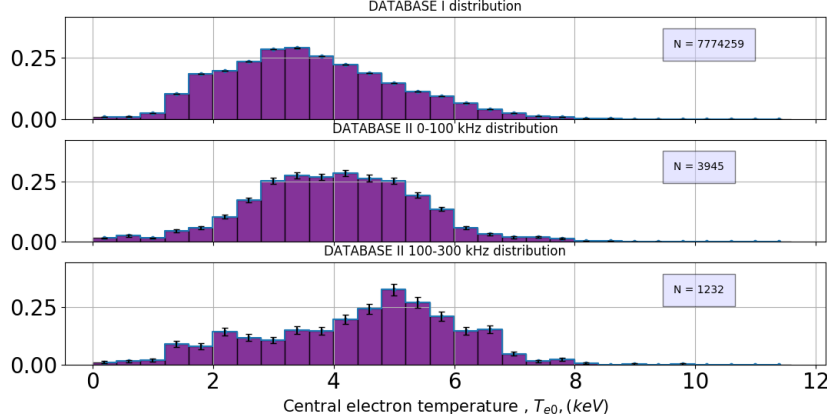


Figure 11: Central electron temperature distribution across databases.

It was interesting to note, for the T_{e0} distribution above, that peaks of the histograms for the low (3.9 keV) and intermediate band (4.4 keV) both display a noticeable shift from the Database I peak (3.6 keV). Given the non-linear dependencies of damping and driving mechanisms on MHD modes [3], it may be difficult to determine the physical origins behind the locations of each peak, with numerical simulation likely required to approach this problem.

4.4.3 Fast ion losses

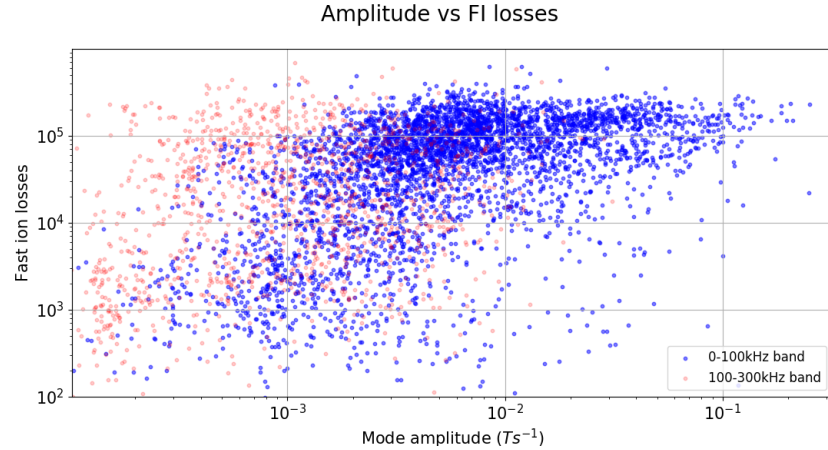


Figure 12: Fast ion losses vs mode amplitude. The trend of interest is in the 0-100kHz band (blue), hence the reason for the faded red scatter points (100-300kHz band).

The KA3 signal; a proxy for fast ion losses in JET that makes use of the interaction between fast ions and charge-coupled devices, displays a non-linear relationship between mode amplitude. In Figure 12 we note that there seems to be a saturation in the KA3 signal once the amplitude of the modes under consideration surpasses $10^{-2.5} T s^{-1}$ (only seen for the low band MHD modes, coloured blue in the figure above). This was an unexpected result, and we hope that future work could look to address this.

5 Conclusion and Opportunities for Further work

This report summarised the methodology behind the creation of two databases that were used to explore trends with MHD mode stability, as well as the subsequent analysis. Entries to Database I provided a pulse overview, whereas Database II entries identified MHD modes displaying instabilities. The procedure by which Database II was compiled (through the application of the MEA; mode extraction algorithm) was overviewed, where it was seen that the (unstable) modes present for a sample pulse (JPN 96851) were *generally* well found, albeit with a small number of false negatives. Future work could aim to formally optimise the thresholds chosen for the MEA, perhaps through the means of the minimisation of a suitably chosen cost function. The MEA should also be adapted to accurately identify all types of MHD modes, such as the RSAE, as well as modes fragmented by sawtooth crashes.

Our analysis of Database II returned results that were generally in agreement with theory and previous experimental data. We highlighted the mode distribution across frequency space, with approximately 5000, 2000 and 200 instabilities identified in 3 clearly discernible bands. The fact that only the thermal population of the plasma is needed to drive modes commonly seen in the low frequency space (the NTM and BTG are examples) is given as potential justification for this trend. Mode stability was seen to depend on normalized plasma plasma beta, β_N , where our results verified that large β_N leads to the destabilization of the low frequency band but stabilization of the intermediate band. Figure 9a agreed with equation 4 for the ‘most unstable’ toroidal mode number in JET¹⁹, with $n = 5$ returned both times. A proxy for the gradient of the fast ion distribution would be insightful, to determine the reason for the increasing trend seen between $q = m/n = 2$ and $q = m/n = 3$ in Figure 9b. An exploration into both the shifted peak trends seen in the T_{e0} distribution (Figure 11), and the apparent saturation of fast ion losses seen in Figure 12 may also be worthwhile.

In coming months we aim to add more pulse data to Database I which will give greater numbers of identified MHD instabilities in Database II. Recent and/or ongoing H, T and DT JET campaigns could provide this, which would allow the 300-500 kHz frequency band (and potentially the 500-1000kHz band) to be explored.

¹⁹Subject to estimations of the terms in equation 4

A Appendix: Coherence calculation

When analysing data from multiple diagnostics that are all recording signals resulting from the same physical phenomenon, it is useful to consider only the signals that are observed by all, or at the very least the majority, of the probes. Such a circumstance occurs in this study, in which we are interested in studying magnetic perturbations resulting from Alfvén and additional MHD modes; low amplitude signals that are not seen by a significant fraction of probes, and of course random noise, are not required for the analysis. To ensure that such effects are not accounted for in further calculations, we quantify the coherence, C , between signals recorded by different probes, and remove the points in our spectrogram that fall below a certain threshold of C . The method of quantification of coherence is discussed now.

Let us begin with two discrete time signals, \vec{x} and \vec{y} ; as with the magnetics signals we apportion the elements into time bins of arbitrary length and perform a Fourier decomposition on each bin. From this we obtain the spectrogram matrices, F^x and F^y respectively, and whilst no frequency and time intervals or resolutions have been explicitly stated yet, we let F_{jk} denote the Fourier coefficient of the j th frequency bin in the k th time bin. We now define the normalised cross spectrum matrix, Cr^{xy} , between \vec{x} and \vec{y} as:

$$Cr^{xy} = \frac{F^x \bar{F^y}}{|F^x| |F^y|} \quad (5)$$

Recalling that the Discrete Fourier Transform decomposes a signal into a finite number of Fourier frequencies²⁰, one can see that the jk th element of Cr^{xy} takes the form $e^{i\theta}$, where θ is the phase difference between the j th Fourier mode of \vec{x} and \vec{y} in the k th time bin. We now state that in order for two signals to display similar structure in time, as would be expected from two of the fast magnetics probes in JET measuring AEs, we require that the phase difference between the two signals stays roughly constant over a number of time bins. Based on this premise we can now define the jk th element of the Coherence matrix between x and y , C_{jk}^{xy} as:

$$C_{jk}^{xy} = \left| \frac{\sum_{l=k-m}^k Cr_{jl}^{xy}}{m} \right| \quad (6)$$

where m is a free parameter given now. Equation (6) can be interpreted as the degree to which the phase difference between the j th Fourier modes of \vec{x} and \vec{y} remains constant over m time bins. If, in this time period the modes maintain a constant phase difference, C_{jk}^{xy} will be exactly one whereas a $C_{jk}^{xy} \approx 0$ is obtained for two modes with little similarity in their structure over m time bins (as stated in section 3, we only analysed signals with coherence > 0.6 .) Section 3, discusses an averaging of coherence calculations over N probes. Here we took N probes and then averaged over all possible coherence matrices (i.e if C_j is the coherence matrix for the j th pairing chosen from k probes, the averaged coherence matrix, C_{avg} is given by $C_{avg} = \sum_{j=1}^{N \choose 2} C_j$. This eliminates other noisy effects that survive the initial coherence calculation. One can think of this last step as ensuring that our spectrogram contains the signals that all N probes ‘see’, as supposed to the signals that are observed by just two probes.

²⁰The j th Fourier frequency for a discrete time signal split into time bins of length T_{bin} is given as $f_j = (j - 1)/T_{bin}$

References

- [1] H. Alfvén. Existence of Electromagnetic-Hydrodynamic Waves. *Nature*, Vol. 150, No. 3805, 1942, pp. 405-406, 1942.
- [2] Fasoli ATesta DSharapov S et al. MHD spectroscopy. *Plasma Physics and Controlled Fusion*, (2002), B159-B172, 44(12B), 2002.
- [3] J.Seo et al. Parametric study of linear stability of toroidal Alfvén Eigenmodes in JET and KSTAR. *Nucl. Fusion* 60 066008, 2020.
- [4] W.W.Heidbrink et al. Stability of beta-induced Alfvén eigenmodes (BAE) in DIII-D. 2020.
- [5] Sergei Gerasimov. JET Magnet Diagnostics. <https://users.euro-fusion.org/pages/mags/experiment/diagnostics-files/diag.html>.
- [6] W. W. Heidbrink. Alpha particle physics in a tokamak burning plasma experiment. *Physics of Plasmas*, (2002), 2002.
- [7] A. Hood. The Lorentz Force - Magnetic Pressure and Tension.
- [8] Kramer. G J. Magnetic safety factor profile before and after sawtooth crashes investigated with toroidicity and ellipticity induced Alfvén eigenmodes. *Nuclear Fusion*, (2001), 41(1135), 2001.
- [9] A.Fasoli M.Porkolab S.Dowson N.Fil P.G.Puglia R.A.Tinguely JET Contributors, D.Testa. Results from the Alfvén Eigenmode Active Diagnostic during the 2019-2020 JET deuterium campaign. *Plasma Phys. Control. Fusion*, (2020), 11, 62.
- [10] K.L.Wong. A review of Alfvén eigenmode observations in toroidal plasmas. *Plasma Physics and Controlled Fusion*, 1999.
- [11] Max Planck Institute for Plasma Physics. Ion Cyclotron Resonance Heating. <https://www.ipp.mpg.de/3871973/ICRH>.
- [12] Blanchard P et al Puglia P, Pires de Sa W. The upgraded JET toroidal Alfvén eigenmode diagnostic system. *Nuclear Fusion*, 2016, 11202, 56(11), 2016.
- [13] T.Bohm S Bourguignon, H.Carfantan. SparSpec: a new method for fitting multiple sinusoids with irregularly sampled data. 2007.
- [14] Y Todo. Introduction to the interaction between energetic particles and Alfvén eigenmodes in toroidal plasmas. *Reviews of Modern Plasma Physics*, (2019), 1, 3, 2019.
- [15] W.W.Heidbrink. Basic physics of Alfvén instabilities driven by energetic particles in toroidally confined plasmas. *Physics of Plasmas* 15, 055501 (2008), 2008.
- [16] Ž. Štancar. Analysis of Neutron Diagnostic Systems in Large Tokamaks. *PhD thesis, University of Ljubljana, Faculty of Mathematics and Physics*, 2019.